Clim Dyn (2012) 39:2937–2955
DOI 10.1007/s00382-012-1324-1

Impact of climate change on mid-twenty-first century growing seasons in Africa

Kerry H. Cook · Edward K. Vizy

Received: 16 September 2011 / Accepted: 20 February 2012 / Published online: 2 March 2012
© The Author(s) 2012. This article is published with open access at Springerlink.com

Abstract Changes in growing seasons for 2041–2060 across Africa are projected using a regional climate model at 90-km resolution, and confidence in the predictions is evaluated. The response is highly regional over West Africa, with decreases in growing season days up to 20% in the western Guinean coast and some regions to the east experiencing 5–10% increases. A longer growing season up to 30% in the central and eastern Sahel is predicted, with shorter seasons in parts of the western Sahel. In East Africa, the short rains (boreal fall) growing season is extended as the Indian Ocean warms, but anomalous mid-tropospheric moisture divergence and a northward shift of Sahel rainfall severely curtails the long rains (boreal spring) season. Enhanced rainfall in January and February increases the growing season in the Congo basin by 5–15% in association with enhanced southwesterly moisture transport from the tropical Atlantic. In Angola and the southern Congo basin, 40–80% reductions in austral spring growing season days are associated with reduced precipitation and increased evapotranspiration. Large simulated reductions in growing season over southeastern Africa are judged to be inaccurate because they occur due to a reduction in rainfall in winter which is over-produced in the model. Only small decreases in the actual growing season are simulated when evapotranspiration increases in the warmer climate. The continent-wide changes in growing season are primarily the result of increased evapotranspiration over the warmed land, changes in the intensity and seasonal cycle of the thermal low, and warming of the Indian Ocean.

Keywords Growing season · Climate change · Africa · Precipitation · Potential evapotranspiration · Regional climate model · Growing season days · Climate change impacts

K. H. Cook (✉) · E. K. Vizy
Department of Geological Sciences, Jackson School of Geosciences, The University of Texas at Austin, 1 University Station C1100, Austin, TX 78712, USA
e-mail: kc@jsg.utexas.edu

1 Introduction

A reliance on rain-fed agricultural across Africa increases the population's vulnerability to climate variability and change. Improvements in understanding and predicting future changes in the growing season will allow for better planning and help mitigate impacts.

The timing of growing seasons varies greatly across this large continent, which spans the tropics and subtropics of both hemispheres and contains 20% or the earth's land surface area, so a regional approach is needed. The purpose of this study is to predict changes in growing seasons, expressed in terms of growing season days (GSDs), for mid-century (2040–2060) due to changes in atmospheric greenhouse gas levels. A regional climate model is used, constrained by reanalysis and output from coupled GCM simulations. Emphasis is placed on regionally-specific analysis and the evaluation of confidence in the projections.

Background on previous work to study the relationship between climate and African growing seasons is reviewed in Sect. 2. The regional climate model description and experimental design are presented in Sect. 3a. The method used to calculate growing season is presented in Sect. 3b, and the evaluation of confidence is address in Sect. 3c. The simulations are validated against observations in Sect. 4, and projections of growing season changes are presented

and evaluated in Sect. 5. Conclusions are summarized in Sect. 6.

2 Background

A variety of techniques to estimate African growing season length from climate information have been developed, including precipitation-only based models (e.g., Sivakumar 1988; Odekunle 2004; Segele and Lamb 2005) and precipitation-potential evapotranspiration (PET) models (e.g., Thornthwaite 1948; Cocheme and Franquin 1967; Benoit 1977; FAO 1978).

Precipitation-only models define the growing season(s) using precipitation threshold criteria that can vary regionally, and are useful because rainfall observations are generally available (Stern and Coe 1982). Sivakumar (1988) defines onset over Burkina Faso and Niger as the date after May 1st when the 3-day accumulated rainfall exceeds 20 mm and no dry spells within the next month exceed 7 days. Cessation is defined as the date after 1 September when no rain occurs for 20 days. Odekunle (2004) defines onset (cessation) over Nigeria as the date when an accumulated 7–8% (90%) of the annual rainfall total is obtained for a given station. Segele and Lamb (2005) find that regionally-specific onset and cessation definitions are needed over Ethiopia due to complex orography and high variability. For wetter regions, onset is defined as the date when the 3 day accumulated rainfall is greater than 20 mm provided there are no dry spells within the next month longer than 8 days. In the northern Rift Valley and the eastern lowlands, onset is defined when daily rainfall first exceeds 10 mm. Likewise, the cessation date over wet (dry) regions is taken as the first day of a dry period that lasts for at least 20 (15) days.

An alternative approach uses a water balance model that compares precipitation to PET, with growing season onset defined when precipitation exceeds one half of the PET. Half of PET is used as a threshold to take into account that the actual evapotranspiration rate is smaller than the PET rate (Benoit 1977). Cessation is defined when precipitation remains below ½PET for a specified time. Benoit (1977) used this method to estimate growing season onset over Nigeria and found that an additional criterion was needed to account for false onsets, namely, that a dry spell of 5 days or longer could not begin in the first week of the growing season.

The Food and Agriculture Organization (FAO) of the United Nations (FAO 1978) applied Benoit's (1977) method over Africa using monthly station data. Additional growing days were added at the end of the season to account for soil water storage after precipitation falls below the ½PET threshold.

Thornton et al. (2009, 2011) define growing season length using the ratio of evapotranspiration (ET) to PET. PET is calculated based on the method of Linacre (1977) and depends on temperature, dew-point temperature, and latitude. Growing season onset is defined when ET/PET exceeds 0.8 for 5 consecutive days, and growing season termination is defined when ET/PET is less than 0.5 for 8 consecutive days. This approach is applied to downscaled coupled GCM output (Thornton et al. 2011) to project greater than 20% loss in the length of the growing season over much of the Sahel by the end of the twenty-first century, with smaller losses south of the Sahel. They caution about the uncertainty in the projections, especially over the arid/semi-arid Sahel where the coupled GCM simulations do not validate well in general.

3 Methodology

3.1 Regional climate model simulations

Regional climate model simulations are designed to provide regional-scale information and to provide an opportunity to evaluate the reliability of the projections of climate and growing season. The NCAR/NOAA Weather Research and Forecasting (WRF; Skamarock et al. 2005) regional model V3.1.1 is used with 32 vertical levels, horizontal resolution of 90-km on the Mercator projection, and a time step of 3 min. The top of the atmosphere set at 20 hPa. This resolution is chosen based on previous results (Patricola and Cook 2010, 2011) which demonstrate that the regional model can realistically simulate African climate at this resolution.

Figure 1 shows the full model domain with topography as resolved at 90-km. The large model domain minimizes the effects of lateral boundary constraints in the analysis over Africa and provides ample space for the development of subtropical anticyclones over the oceans.

Physical parameterizations are chosen based on testing, and include the Yonsei University planetary boundary layer (Hong et al. 2006), Monin–Obukhov surface layer, new Kain-Fritsch cumulus convection (Kain 2004), Purdue Lin microphysics (Chen and Sun 2002), RRTM longwave radiation (Mlawer et al. 1997), the Dudhia shortwave radiation (Dudhia 1989), and the unified Noah land surface model (LSM; Chen and Dudhia 2001).

An ensemble approach is used to provide one way of evaluating confidence in the projections, i.e., by examining agreement among ensemble members. Two ensembles, each with 6 members, are generated. The first represents the late twentieth century (1981–2000) as is referred to as "20C". Initial, lateral, and surface boundary conditions for all six ensemble members are derived from the 1981–2000

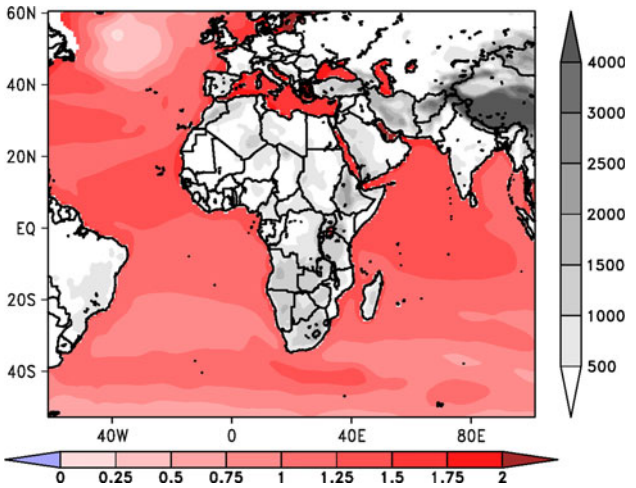

Fig. 1 Regional model domain with topography (meters) and the annual-mean of the SSTAs (K) imposed in the 21C simulation

monthly climatology in the National Centers for Environmental Prediction reanalysis 2 (NCEP2; Kanamitsu et al. 2002), interpolated onto the regional model grid. Lateral boundary conditions for horizontal winds, temperature, relative humidity, and geopotential height are updated every 6 h using the NCEP2 climatological values. The monthly means are assumed to represent the middle of the month, and linear interpolation is used to generate boundary conditions every 6 h. These boundary conditions include seasonality, but shorter timescales are filtered out. This "climate-mode" methodology has proved to be useful for tropical and subtropical regional modeling studies over Africa (Vizy and Cook 2002; Patricola and Cook 2007, 2010, 2011), the Indian Ocean (Vizy and Cook 2003; Hagos and Cook 2007), and the tropical Atlantic and South America (Vizy and Cook 2005, 2010; Cook and Vizy 2008), and simulations on this domain with synoptically-varying boundary conditions confirm the usefulness of this approach.

The 6 20C ensemble members are year-long simulations with different initial conditions. They are taken from 2 to 3-year integrations that are initialized with climatological reanalysis values for different dates, namely, 1 March and 15 March. Each run is spun up until the following 1 January. The 9 (or 9.5) month spinup period is needed to allow soil moisture to equilibrate with the climate. Initial values for soil moisture at the 4 levels required by the LSM are calculated from reanalysis values. For computational efficiency, each of the 6 ensemble members is not spun up individually. The 6 ensemble members are treated as independent annual simulations, and simulations from one 3-year run do not tend to cluster. The 3-hourly output from the six runs is averaged to produce the 20C ensemble mean.

The second ensemble, 21C, represents mid-twenty-first century (2041–2060) conditions under the IPCC AR4 A1B emissions scenario. This is a mid-line scenario for balancing carbon dioxide output and economic growth. The atmospheric CO_2 concentration is increased to 536 ppmv, the 2041–2060 average in the A1B scenario. Effects of other greenhouse gases and aerosols are not included. Boundary conditions for the 21C simulations are derived from coupled GCM simulations and applied as anomalies to the reanalysis boundary conditions. These future GCM anomalies are calculated as differences between monthly-mean, A1B-forced simulations averaged over 2041–2060 and simulations averaged over 1981–2000. The monthly-mean anomalies are interpolated to the NCEP reanalysis grid, and added to the reanalysis climatological monthly averages. Finally, 6-hourly values for the 21C simulations are derived using linear interpolation. Soil moisture initialization values from 20C are used for the 21C simulations, and 6 ensemble members are generated as for the 20C case.

Simulations from nine coupled GCMs prepared as part of the World Climate Research Programme's (WCRP's) Coupled Model Intercomparison Project 3 (CMIP3; Meehl et al. 2007) are used to generate future anomalies. The models used are the Canadian Centre for Climate Modeling and Analysis CGCM3.1(T47), Météo-France/Centre de Recherches Météorologiques CNRM-CM3, Max Plank Institute for Meteorology ECHAM5/MPI-OM, NOAA Geophysical Fluid Dynamics Laboratory GFDL-CM2.0, Center for Climate Research MIROC3.2(medres), Meteorological Research Institute MRI-CGCM2.3.2, National Center for Atmospheric Research CCSM3, National Center for Atmospheric Research PCM, and the Hadley Centre for Climate Prediction and Research/Met Office UKMO-HadCM3. Multi-model mean GCM anomalies are used to reduce the dependence of the projections on any one GCM. Regional model simulations by Patricola and Cook (2010, 2011) yield good agreement over northern Africa in future projections at the end of the twenty-first century among runs forced individually by these 9 GCMs.

Contours in Fig. 1 show the annual mean of the imposed SSTAs derived from the coupled GCM simulations. While SSTs vary seasonally in the simulation, seasonal variations in the anomalies are small. Maximum open-ocean warming within the domain is under 2 K. A low-amplitude Indian Ocean dipole pattern is imposed, and the northern tropical Atlantic Ocean is slightly warmer (by about 0.25 K) than the southern tropical Atlantic.

This approach to simulating future climate with regional models produces projections that are as independent as possible from AOGCM simulations. This is not a traditional downscaling of GCM simulations, and the approach

avoids propagating errors in the twentieth century simulation from GCMs into the regional model domain.

3.2 Growing season calculation

Growing season onset, end, and length are calculated using the FAO method (FAO 1978) described above, but adapted for daily rather than monthly input. Precipitation is taken directly from the regional model simulations. PET is calculated from model output using the Penman–Monteith equation (Allen et al. 1998),

$$PET = \frac{0.408\Delta(R_{net} - G) + \gamma \frac{900}{T_a+273} u_{2m}(e_s - e_a)}{\Delta + \gamma(1 + 0.34u_{2m})} \quad (1)$$

where PET is in mm day^{-1}, Δ is the slope of the saturated vapor pressure–temperature curve (kPa °C^{-1}), R_{net} is the net radiation at the surface (10^6 J m^{-2} day^{-1}), G is the soil heat flux density (10^6 J m^{-2} day^{-1}), γ is the psychrometric constant (kPa °C^{-1}), T_a is the mean daily 2-m air temperature (°C), u_{2m} is the wind speed at 2 m height (m s^{-1}), e_s is the saturation vapor pressure (kPa), and e_a is the actual vapor pressure (kPa). The following quantities are given by

$$\Delta = \frac{2504 \exp\left(\frac{17.27T_a}{T_a+237.3}\right)}{(T_a + 237.3)^2} \quad (2)$$

$$e_s = 0.611 \exp\left(\frac{17.27T_a}{T_a + 237.3}\right) \quad (3)$$

$$e_a = 0.611 \exp\left(\frac{17.27T_d}{T_d + 237.3}\right) \quad (4)$$

where T_d is the mean daily dew point temperature at 2 m (°C), and

$$\gamma = 0.00163 \frac{P}{\lambda} \quad (5)$$

where P is atmospheric surface pressure (kPa) and λ is the latent heat of vaporization (10^6 J kg^{-1}) taken as

$$\lambda = 2.501 - \left(2.361 \times 10^{-3}\right) T_a \quad (6)$$

Before calculating growing season days (GSDs), an 11-day running mean smoothing is applied to the model output. This filters synoptic timescale variations since changes in growing season length due to individual weather events cannot be addressed with this experimental design. The goal is to identify and understand climate-scale growing season changes.

A day when the precipitation is greater than ½PET is a GSD provided that the daily near-surface air temperature is greater than 6.5°C. Growing season onset is defined as the date(s) when the precipitation first exceeds ½PET and the temperature criterion is met. Growing season cessation is the date on which the daily precipitation falls below ½PET, plus the number of days required to evapotranspire an additional 100 mm of water assumed to be stored in the soil, using Eq. 1. The choice of 100 mm is based on empirical evidence over West Africa and East Africa (FAO 1978). If the daily precipitation becomes greater than ½ PET before 100 mm of water is evapotranspired, then the dates are included in the growing season.

3.3 Evaluating confidence

Confidence in the simulations is evaluated by the following methods:

- The quality of the 20C simulation in each region is evaluated, with a reasonable (state-of-the-art) representation of the region's climate seen as a necessary but not sufficient condition for confident prediction.
- Changed hydrological features associated with changes in GSD are identified and the degree of agreement among ensemble members for simulating the change is evaluated.
- The physical processes of a simulated change are studied and compared with features of observed regional variations.
- Results are compared with other modeling studies when available.

4 Model validation

Figure 2a shows the distribution of GSDs over Africa for the twentieth century climate as calculated by the FAO. Over sub-Saharan Africa, e.g., south of 18°N, the number of GSDs increases to south, with the sharpest gradients over the southern Sahel where GSDs increase from less than 30 days to over 180 days from 10°N to 15°N. Over Ethiopia (centered near 10°N and 40°E) the pattern of GSDs reflects topography, with highest values on the western and southern slopes of the Ethiopian Highlands. The maximum number of growing season days occurs in the Congo basin (within about 5° of the equator near 25°E), along the Guinean coast, and along the east coast of Madagascar. Between 15°S and the equator the number of GSDs is generally more than 180 days west of the Rift Valley (~35°E) and ranges between 90 and 180 days over Tanzania, northern Zambia, and northern Mozambique to the west of the Rift Valley. South of 15°S there is a zonal gradient, with less than 30 growing season days along the Atlantic coast of Namibia and South Africa, and 180–210 days along the Indian Ocean coast.

Figure 2b shows the ensemble mean GSDs from the 20C simulation. The overall pattern of GSD distribution is

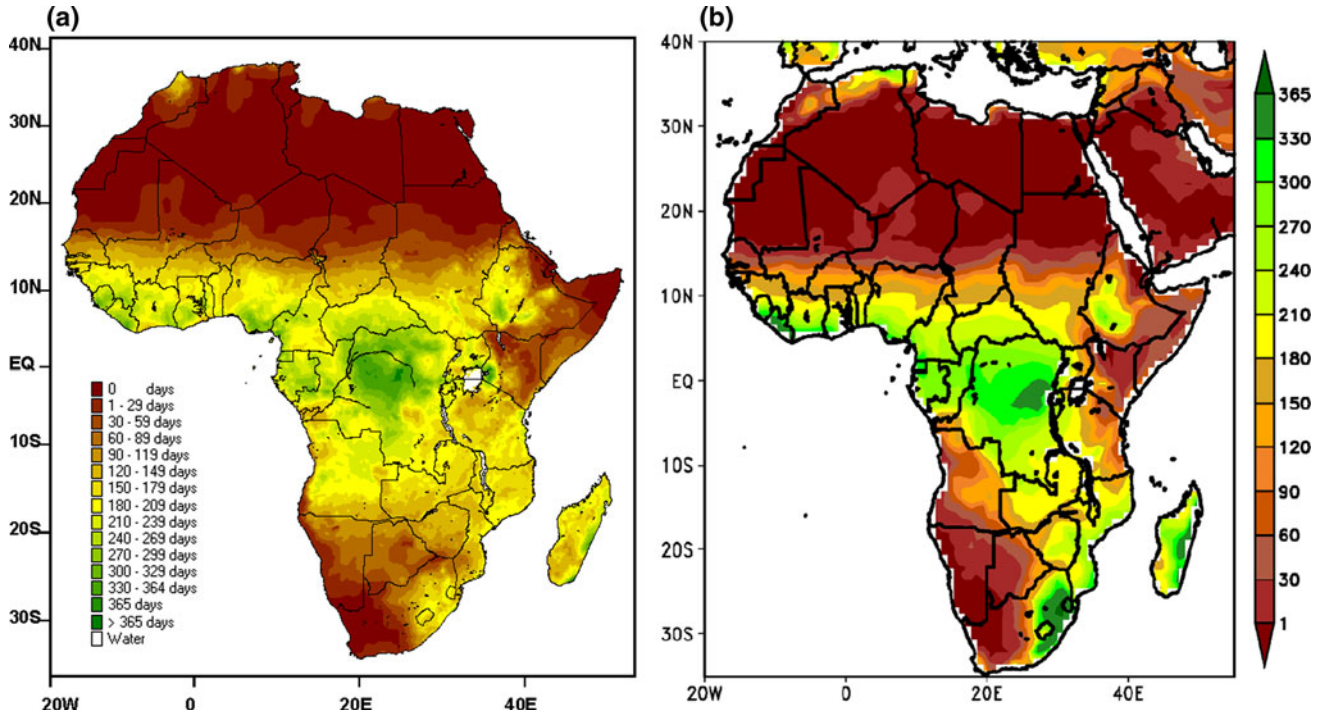

Fig. 2 Calculated growing season days from the **a** Food and Agriculture Organization of the United Nations Natural Resources Climate, Energy, and Tenure Division (FAO/NRC; http://www.fao.org/nr/climpag/cropfor/lgp_en.asp), and the **b** 20C ensemble mean. Note the color scales differ slightly between panels

reproduced by the model, with maximum values in the Congo basin, along the Guinean coast, and the Ethiopian highlands. The pronounced meridional gradients in the Sahel and zonal gradients across southern Africa are also captured in the model, as is the distribution over Kenya, including the Turkana Valley (4°N; 36°E), and the Horn of Africa (Somalia, Ethiopia, Sudan). The Sahel growing zones are placed 2–4° too far south, and the number of growing days is generally overestimated by about 10 days in the tropics. The largest discrepancies between the modeled and FAO-estimated GSDs are along the southeast coast, from Tanzania to South Africa, where the values are too high.

Figure 3a–d show annual rainfall for 4 observational climatologies, and the regional model 20C ensemble mean is shown in Fig. 3e. The model captures the sharp meridional gradients over the Sahel, although the 2 mm/day contour is 1–2° of latitude further south than in the observations, similar to the southward misplacement of the GSD gradient in Fig. 2b. The 20C simulation has a wet bias in the tropics, ranging from 1 to 9 mm/day. The bias is smaller when comparing with the higher-resolution observations (TRMM and CRU). As seen in the following section, over-production of rainfall in the simulation is not unrelated to the over-production of GSDs, but the determination of GSDs is more closely associated with the timing of seasonal variations in rainfall than with the intensity. The largest inaccuracy in the model simulation of precipitation is in the southeastern quadrant of the continent, where a diagonal band of high rainfall rates extends to the southeast from the Congo basin.

The simulation of precipitation is a significant challenge in climate modeling. As a point of reference, Fig. 3f shows the average 1981–2000 precipitation climatology from the coupled GCMs used to generate future boundary condition anomalies. This GCM multi-model mean climatology overestimates rainfall rates in the tropical interior, as does the regional model, but underestimates West African rainfall rates, keeping the precipitation maximum over the Gulf of Guinea instead of over the Guinean coast. Precipitation over southeastern Africa is more realistic than in the regional model, but the southwest is too wet.

In Fig. 4, the TRMM and 20C precipitation climatologies are compared for the traditionally-defined seasons. Even though these 3-month averages may not be the most relevant for all regional growing seasons, the comparison gives an overview of the accuracy of the regional model simulation. In the December, January and February mean (DJF; Fig. 4a, b), the simulated distribution of precipitation is reasonable, but precipitation rates over the central southeast coast and Madagascar are too large. These high austral summer rainfall rates are primarily responsible for the high annual rain (Fig. 3) simulated in this region. Rainfall over the southwest is too low.

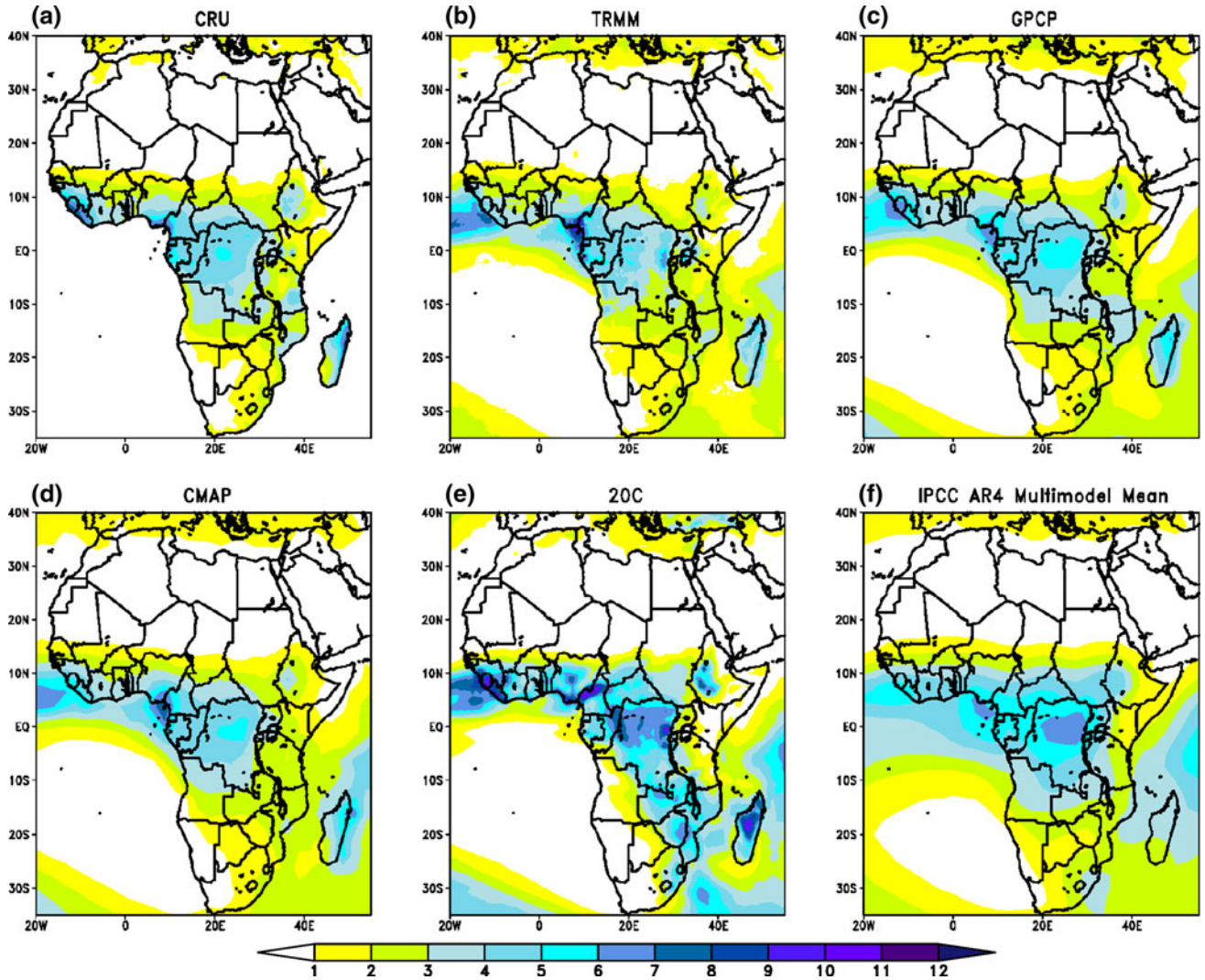

Fig. 3 Annual rainfall rates (mm day^{-1}) from the **a** 1979–2006 CRU TS 3.0 climatology (Mitchell and Jones 2005), **b** 1998–2010 NASA TRMM 3B42V6 climatology (Huffman et al. 2007), **c** 1979–2010 NASA GPCP V2.2 climatology (Adler et al. 2003), **d** 1979–2010 Climate Prediction Center (CPC) Merged Analysis of Precipitation (CMAP; Xie and Arkin 1997), **e** 20C ensemble mean, and **f** IPCC AR4 AOGCM multi-model mean (9-models) averaged 1981–2000

In March through May (MAM; Fig. 4c, d) the observed distribution is again captured well in the model. Rainfall moves toward the north, with maximum values close to the equator during this transition season. Rainfall over the Guinean coast and the Ethiopian highlands has begun, but again rates are somewhat high.

The northward excursion of rainfall continues in both the observations and model in the June, July and August average (JJA; Fig. 4e, f). The overproduction of rain is again quite pronounced, but the distribution is accurate. In particular, the rainfall maximum over West Africa has moved into the Sahel leaving a summer minimum along the Guinean coast, and most of the east coast experiences the observed summer dry period as well.

In September, October and November (SON; Fig. 4g, h) the Southern Hemisphere rainy season begins and the rainfall maximum is again close to the equator. As in the observations, the simulated rainfall over the Congo basin is greater than in boreal spring.

Surface air temperature in the regional model is compared with the ERA-Interim reanalysis (1989–2009; Dee et al. 2011), along with the low-level (850 hPa) flow. In DJF (Fig. 5a, b), the model exhibits a warm bias of 2–4 K over sub-Saharan Africa, but the structure of the temperature field is reasonable. Northeasterly (Harmattan) flow over sub-Saharan northern Africa is captured, as are the northeasterly winds of the Asian winter monsoon that flow across the Horn of Africa. The South Atlantic subtropical

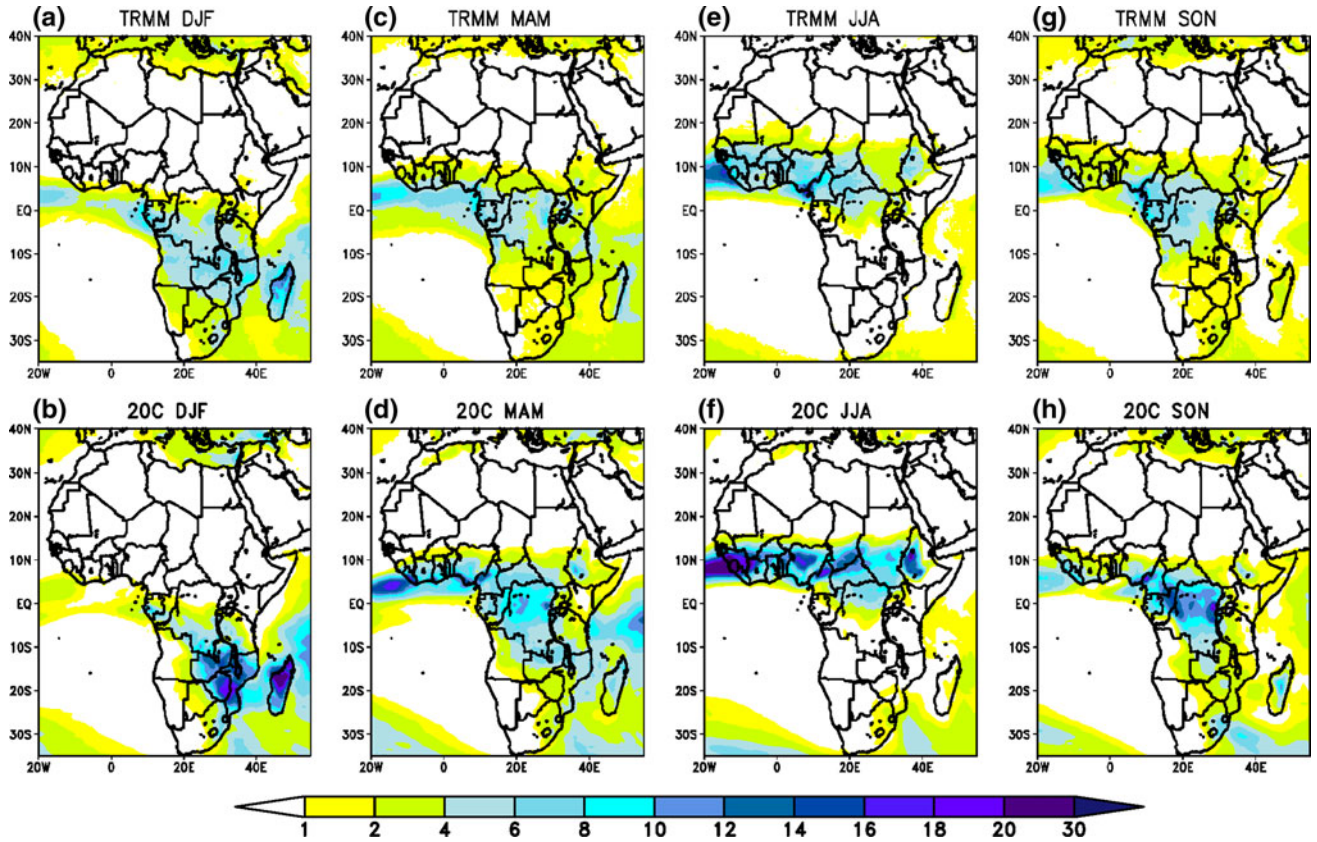

Fig. 4 December–February rainfall rates from the **a** 1998–2010 NASA TRMM 3B42V6 climatology (Huffman et al. 2007) and **b** 20C ensemble mean. March–May rainfall from **c** TRMM and **d** 20C. June–August rainfall from **e** TRMM and **f** 20C. September–November rainfall from **g** TRMM and **h** 20C

high is fairly well placed in the simulation, but the observed onshore easterly flow between 20°S and 30°S is not produced in the model.

The simulation of surface air temperature in MAM is accurate, with only a small (∼1 K) warm bias in the southern continental interior and parts of East Africa. Similarly, the low-level flow field is represented well in the model in MAM.

The southern continental interior and parts of East Africa continue with a small warm bias, up to 1.5 K, into JJA, but otherwise the surface air temperature simulation is reasonable. The Somali jet forms off the east coast, as does the onshore flow of the West African monsoon (below 850 hPa; not shown). The warm bias is also present in the SON simulation (Fig. 5g, h), mostly in the Southern Hemisphere. Winds speed over the equatorial Atlantic, subtropical southern Africa, and the Sahel are somewhat strong.

While the RCM simulation of the late twentieth century climate is not perfect, the regional model is clearly capable of producing a reasonable, state-of-the-art simulation of the African climate, including its seasonality. In particular, the simulation of the distribution of GSDs is quite similar to that of the FAO estimate, with the possible exception of the southeastern coast of Africa (discussed below).

5 Results

Figure 6a shows the projected change in the number of GSDs for 21C compared with 20C, and Fig. 6b displays the change as a percentage of the 20C growing season. Some regions lose the majority of the growing season and other regions experience significant increases. Because of this regionality the analysis focuses on individual regions.

5.1 West Africa and the Sahel

Changes in GSDs vary over West Africa (Fig. 6). West of the Greenwich meridian, growing days decrease by up to 30 days (20%) over a large region including Guinea, Sierra Leone, Guinea Bissau, Côte d' Ivoire, Burkina Faso, and southern Mali. In the northern part of this region, the western Sahel, these decreases essentially eliminate the growing season. GSDs increase to the west (Ghana, Togo, Benin) by 1–2 weeks (5–10%). Increases in GSDs over

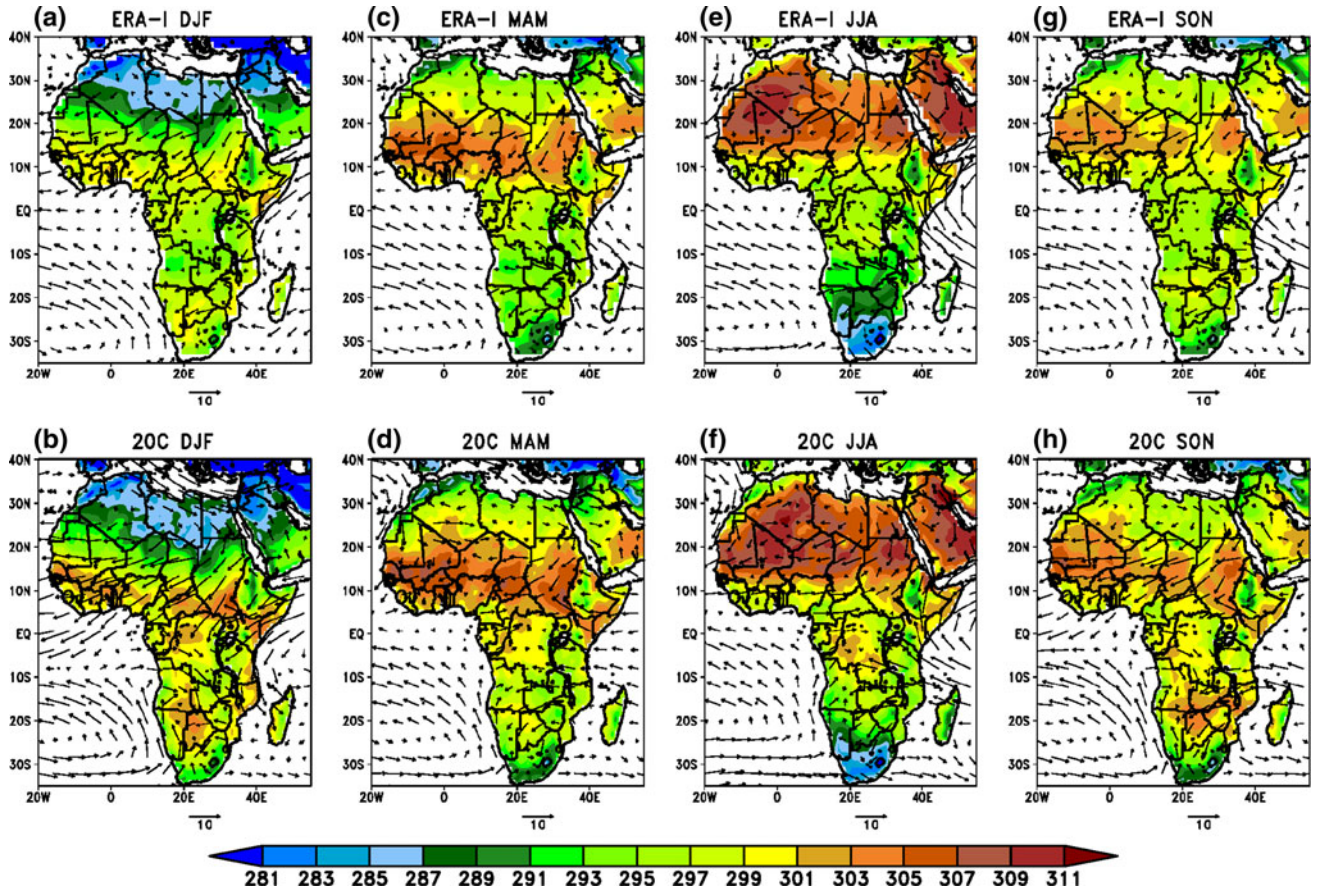

Fig. 5 Seasonal surface air temperature (K) and 850-hPa winds (vectors; m/s) from the (*top row*) 1989–2009 ERA Interim climatology and (*bottom row*) 20C ensemble mean

Senegal and western Mali are generally under 5 days (10%). A coherent signal emerges across the central and eastern Sahel near 15°N, with increases in GSDs up to 20 days, or 30%, and some regions (indicated by purple in Fig. 6b) attaining growing season days in the 21C simulation where there were none in the 20C simulation.

Figure 7a shows the annual time series of precipitation and ½PET for the 20C and 21C ensemble means averaged over 8.3 N–11.7 N and 14.9 W–4.6 W, the region of strongest decreases in GSDs (Fig. 6). In the 20C simulation, the rainy season begins in the beginning of May but in the 21C simulation it is delayed until the end of May, with good agreement in this response among the ensemble members (not shown). PET is increased over this region during the first half of the year in the mean as well as in each ensemble member (not shown), especially during May when soil moisture values are reduced in the 21C case. Because of these positive PET and negative precipitation anomalies during May, the growing season is shortened by about 4 weeks. Note that in June, July, and August rainfall rates in the 21C case are greater than those in the 20C case, but these increases do not affect the number of GSDs.

To the east of this region of decreased GSDs there is an increase in GSDs that is also associated with changes in spring rainfall. Figure 7b shows precipitation and ½PET for the 20C and 21C simulations averaged over 8°N–11.5°N and 0–9E. In this region, an enhancement in spring rainfall, with very little change in PET, increases the annual count of GSDs.

Moisture transport anomalies (vectors) and geopotential height anomalies (contours) at 900 hPa are shown in Fig. 7c along with precipitation anomalies (shaded) for May. Southwesterly flow anomalies carry moisture from the region with negative precipitation anomaly into and beyond the region with a positive anomaly. The anomalous flow is directed down the anomalous geopotential height gradient, toward the Sahara. Negative geopotential height anomalies to the northeast of the precipitation anomalies indicate that the Saharan heat low is strengthened in the 21C simulation compared with 20C.

Figure 8a shows the annual cycle of precipitation and ½PET for the central and eastern Sahel (12.5°N–16.7°N; 4.9°E–42.0°E) in the 20C and 21C simulations. The ½PET time series is bimodal, with minima during the cool period

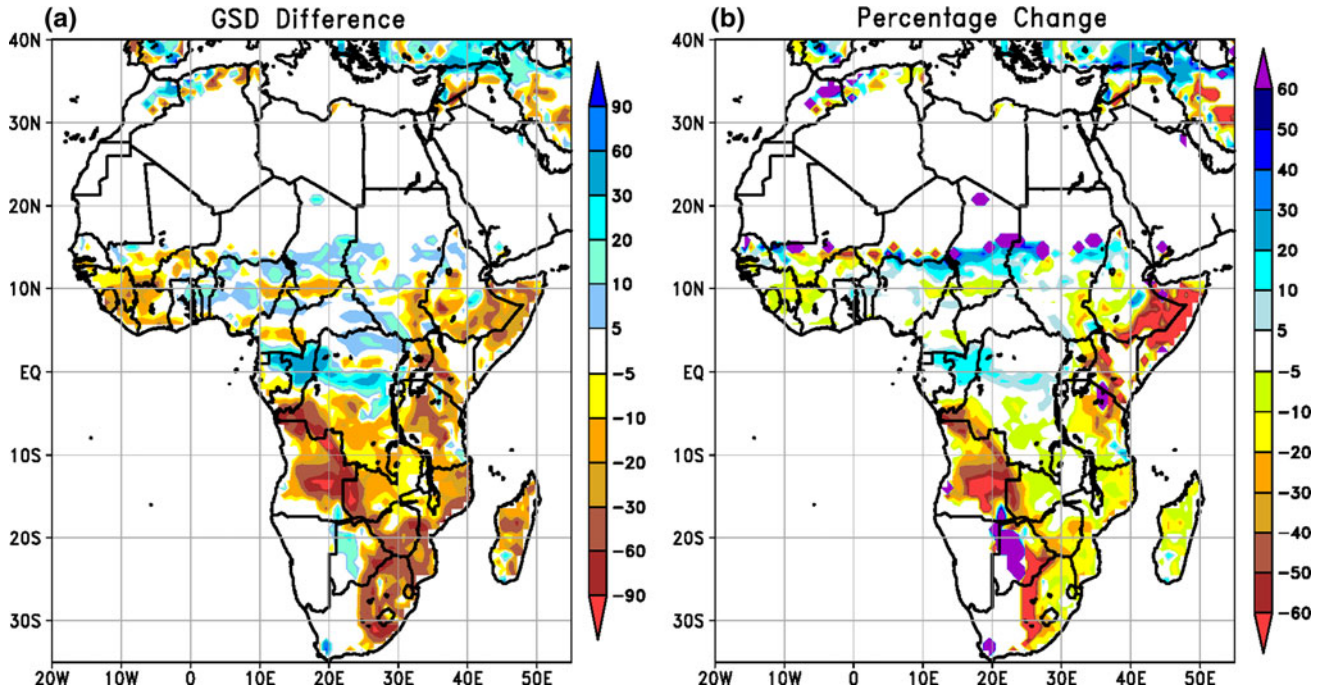

Fig. 6 Difference in growing season days (21C–20C) expressed as the number of days and **b** as a percent change from the number of days in the 20C ensemble-mean value at each grid point

(Jan) and the wet season (Aug). It increases in the 21C simulation compared with the 20C simulation by about 1 mm/day except when the soil is moist from the 1st week in August until the middle of September. Growing days accumulate in the summer in the Sahel, when precipitation rates increase and PET rates decrease. The cause of the increase in GSDs in the 21C simulation is a summer precipitation enhancement of 1–2 mm/day.

Figure 8b shows precipitation anomalies for 21C–20C averaged over July and August along with 900-hPa moisture transport and geopotential height anomalies. Despite an overall increase in geopotential heights in the greenhouse gas-warmed world, the thermal low is about 2 gpm deeper in the 21C simulation compared with the 20C simulation and negative geopotential gradients across the Sahel are enhanced. An anomalous southwesterly flow with a strong ageostrophic component directed down the geopotential height gradient is generated, converging over the Sahel to support the precipitation increases. As seen in Fig. 8c, the strengthening of the thermal low is associated with a surface temperature anomaly of 2–3 K north of 15°N. To the south, the temperature anomaly is much smaller due to the increased precipitation and soil wetness. It is likely that this feedback from the land surface, through the influence of soil moisture on surface temperature, enhances the meridional temperature and geopotential height gradients in the southern Sahel.

To summarize changes in GSDs simulated for West Africa and the Sahel, exact start and end dates for the growing season are noted for the averaging regions in the 20C and 21C simulations in Table 1. The extension to the growing season due to water storage in the soil past the date on which precipitation falls below ½PET is included. Reductions in the extension times occur because surface temperatures are generally warmer but the changes are not large, amounting to only 1–2 days. These dates only provide a general characterization of the changes since the number of GSDs will vary significantly within the region, the dates will vary somewhat depending on the averaging region used, and because the model simulation cannot be expected to capture the exact dates, which are not even known precisely from observational records.

Confidence in the projected changes in GSDs in West Africa and the Sahel is heightened by the good validation of the regional climate (Figs. 3, 4, 5, 6) and by agreement in the precipitation responses across the ensemble members. All 6 21C ensemble members produce the delayed monsoon onset (i.e., May precipitation reductions) in the western West Africa region in the sense that May precipitation in all 6 21C simulations is below the 20C May mean. Even more stringently, all of the 6 21C simulations for May produce less precipitation than 5 out of 6 of the 21C simulations. The early onset in the eastern West Africa region and the central/eastern Sahel is similarly robust across the ensemble members.

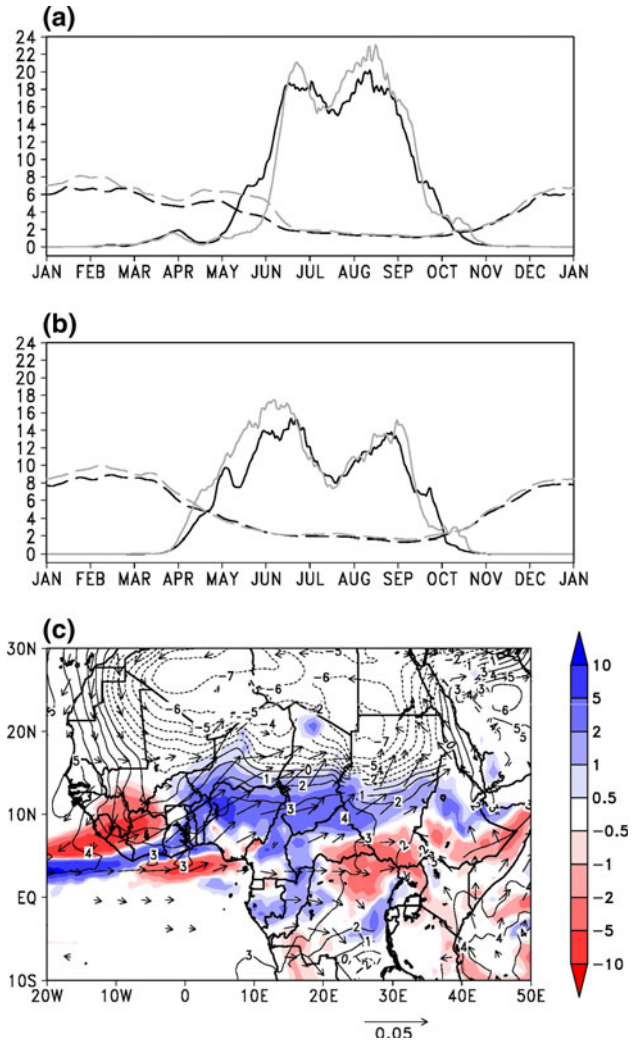

Fig. 7 Annual time series of precipitation (*solid*) and ½PET (*dashed*) over **a** western West Africa averaged 14.9°W–4.6°W and 8.3°N–11.7°N and **b** eastern West Africa averaged 0.2°W–9.2°E and 8.3°N–11.7°N from the 20C (*black*) and 21C (*gray*) ensemble means. **c** May precipitation (mm/day), 900-hPa qv (kg m/kg s), and geopotential height anomalies for 21C–20C. Anomalous vectors with magnitudes less than 0.005 kg m/kg s are not plotted

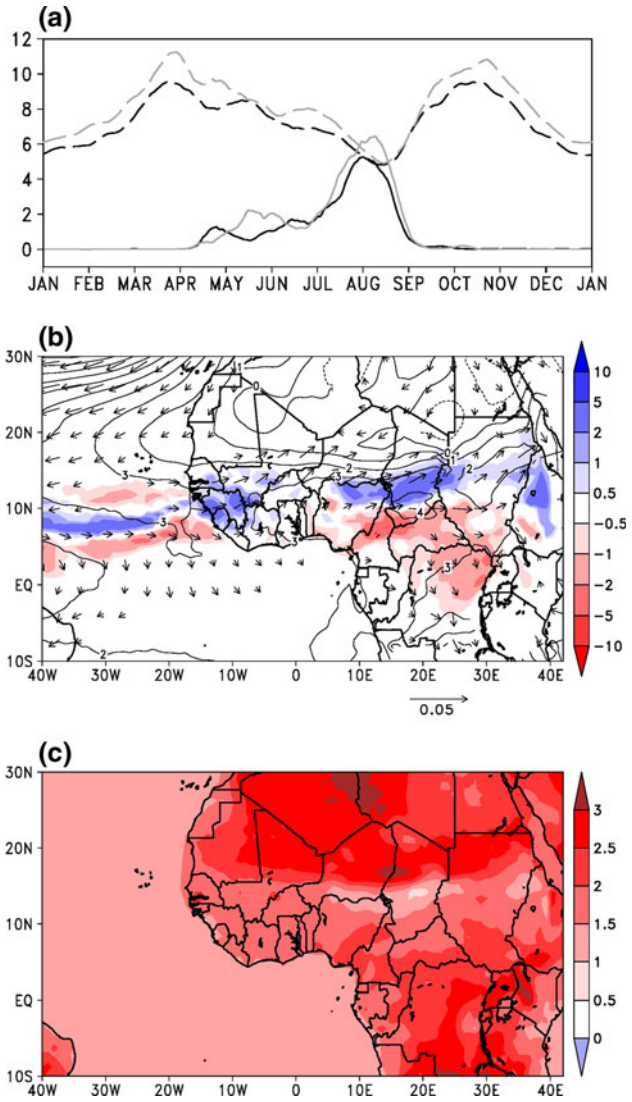

Fig. 8 **a** Annual time series of precipitation (*solid*) and ½PET (*dashed*) in the Central/Eastern Sahel averaging region (4.9°E–42.0°E and 12.5°N–16.7°N) from the 20C (*black*) and 21C (*gray*) ensemble means. **b** July/August 21C–20C precipitation (mm/day), 900-hPa moisture transport (kg m/kg s), and 900 hPa geopotential height anomalies. **c** July/August 21C–20C surface temperature differences (K)

The regional changes in GSDs over West Africa and the Sahel are related to a simulated strengthening of the Saharan heat low in boreal spring and summer. Several physical mechanisms could be responsible. Direct CO_2 forcing in the dry atmospheric column, where increases in atmospheric greenhouse gases provide a high-percentage increase in the longwave back radiation, warm the surface. There may also be enhanced subsidence over the Sahara associated with an early onset of the Indian monsoon (Rodwell and Hoskins 2001) and/or warming in the Indian Ocean (Hagos and Cook 2008). The present simulations do not allow a definitive attribution, since this would require repeated simulations applying each forcing function individually, and the net result would not likely be a linear superposition of the individual responses. However, the present analysis suggests that each of these mechanisms is playing a role in the deepening of the thermal low.

GCM projections from the AR4 did not produce a strong annual precipitation response over West Africa and the Sahel (Cook 2008), and they do not resolve the regional response on the space scales evaluated here. However, Biasutti and Sobel (2009) find a delayed monsoon onset in many of the GCM simulations, consistent with the May reduction in rainfall simulated here for the western West African region. In regional-scale simulations for 2081–2100 under the stronger forcing of the SRESA2

Table 1 Simulated changes in growing seasons over West Africa and the Sahel

Region/season		Start date ($P > 1/2$PET)	End date ($P < 1/2$PET)	Extension[a]	Difference (21C–20C)
Western West Africa	20C	May 13	October 13	November 6	−18 days
	21C	June 4	October 21	November 10	
Eastern West Africa	20C	April 22	October 3	October 22	+14 days
	21C	April 14	October 13	October28	
Central and eastern Sahel	20C	August 2	August 10	August 20	+10 days
	21C	July 30	August 18	August 27	

[a] Estimated date following the date when precipitation falls below 1/2PET on which 100 mm of water stored in the soil has evapotranspired

scenario, Patricola and Cook (2010) find a zonally-uniform response over West Africa, with wet conditions along the entire Guinean coast in May and drying across West Africa and the Sahel in June and July. This may represent disagreement with the present simulations or it may indicate that the response of the West African monsoon is nonlinear. Neupane and Cook (2012) find that Atlantic SSTAs of 2 K or less produce increased precipitation in the Sahel, while warming above 2 K produces drying. This is consistent with Vigaud et al. (2011), who downscale GCM projections for 2032–2041 over northern Africa. With the relatively small SSTAs of this time period, they also find that Sahel rainfall is increased in the summer, primarily due to a delayed end to the season.

5.2 Greater Horn of Africa (GHA)

According to Fig. 2, the growing season across most of the GHA (roughly 12°S–12°N and 30°W–50°W, including Sudan, Eritrea, Djibouti, Ethiopia, Somalia, Uganda, Kenya, and Tanzania) is relatively short except along the western and southern slopes of the Ethiopian highlands. Large decreases in GSDs are simulated across the region in 21C (Fig. 6). Growing days are essentially eliminated in eastern Ethiopia and Somalia, and the number of GSDs is reduced by 10–40% over much of Tanzania, with greater reductions over southern Kenya.

Two separate East African regions are examined. One covers eastern Ethiopia and Somalia (43.7°E–53.2°E and 4.0°N–11.7°N), and the other much of Tanzania and southern Kenya (29.9°E–44.6°E and 11.4°S–3.1°N). These GHA regions are investigated separately because they have different growing seasons and climate dynamics, and because they are separated by a region with no change in GSDs over northern Kenya (Fig. 6).

Area-averaged, ensemble-mean precipitation and ½PET for these two regions in the 20C and 21C simulations are shown in Fig. 9a and b, respectively. Both regions experience two rainy seasons in the 20C simulation, as seen in Fig. 4 as well. The boreal spring season is known as the "long rains", and the "short rains" occur in boreal fall. The long-rains occur earlier in Tanzania/southern Kenya than in eastern Ethiopia/Somalia in the simulation, and the short-rains are later, as is observed. In both regions, GSDs are generated in the spring when precipitation rates exceed ½PET. In the fall, precipitation exceeds ½PET for about 3 weeks for the area average over Tanzania and southern Kenya (Fig. 9b), indicating the presence of a second growing season. In reality, the viability of a second growing season depends on some of the finer-scale topographic and hydrological features in the regions, and areas of both GHA domains have bimodal growing seasons (Corbett et al. 1995; Thornton et al. 2009).

In both GHA regions ½PET increases by about 1 mm/day throughout the year in the 21C simulation (gray lines in Fig. 9a, b), reducing GSDs in both regions during both growing seasons. The spring growing season in eastern Ethiopia/Somalia is further reduced (to zero in the area average) because precipitation rates are halved in the 21C simulation. In the Tanzania/southern Kenya region precipitation is reduced by about 25%, bringing rainfall below ½PET and eliminating the long-rains growing season (in the area average).

In boreal fall, PET increases over eastern Ethiopia/Somalia are accompanied by small precipitation increases and there is a reduction in surface water availability. Over Tanzania/southern Kenya, the magnitude and duration of the short rains is extended and the growing season is extended by 49 days. Simulated start and end dates for the growing season in the two East African regions are listed in Table 2.

Figures 3, 4, 5 indicate that the 20C simulation captures the region's precipitation and surface temperature fields reasonably well, and this supports confidence in the projections. Figure 9c and d display time series of precipitation for the eastern Ethiopia/Somalia and Tanzania/southern Kenya regions, respectively, from each of the 6 20C (black lines) and the 6 21C ensemble members (gray lines). For the precipitation reduction in May over eastern Ethiopia/Somalia, 5 of the 6 21C ensemble members produce rainfall rates that are less than the 20C mean. Note that one of the 21C ensemble members produces very

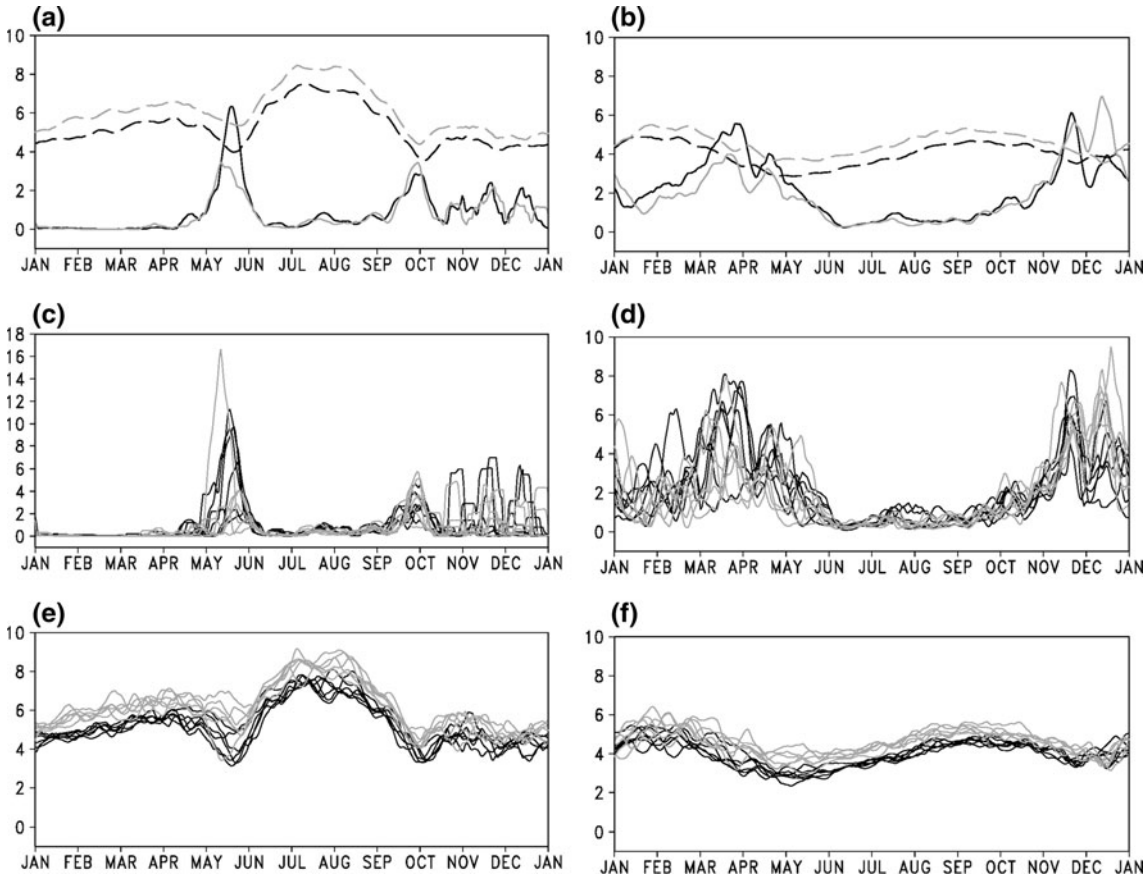

Fig. 9 Annual time series of precipitation (*solid*) and ½PET (*dashed*) over **a** eastern Ethiopia/Somalia averaged 43.7°E–53.2°E and 4.0°N–11.7°N and **b** southern Kenya/Tanzania averaged 29.9°E–44.6°E and 11.4°S–3.1°N from the 20C (*black*) and 21C (*gray*) ensemble means. Time series of precipitation over the **c** eastern Ethiopia/Somalia and **d** southern Kenya/Tanzania regions from each 20C (*black*) and 21C (*gray*) ensemble member. Time series of ½PET over the **e** eastern Ethiopia/Somalia and **f** southern Kenya/Tanzania regions from each 20C (*black*) and 21C (*gray*) ensemble member. All values have been smoothed using an 11-day running mean

Table 2 Simulated changes in growing seasons over the Greater Horn of Africa

Region/season		Start date ($P > 1/2PET$)	End date ($P < 1/2PET$)	Extension[a]	Difference (21C-20C)
Somalia/eastern Ethiopia	20C	May 15	May 27	June 6	−22 days
	21C	None	None	None	
Tanzania/southern Kenya: Spring long rains	20C	March 11	April 30	May 17	−68 days
	21C	None	None	None	
Tanzania/southern Kenya: Fall short rains	20C	November 14	November 28	December 10	+49 days
	21C	November 14	December 22	January 2	

[a] Estimated date following the date when precipitation falls below 1/2PET on which 100 mm of water stored in the soil has evapotranspired

strong rainfall, consistent with the idea that climate change will bring increases in climate variability and extreme events. Over Tanzania/southern Kenya, 5 of the 6 21C ensemble members produce rainfall rates averaged over March and April that are less than the 20C ensemble mean, which also supports confidence in the simulation. The extension of the short rains season over Tanzania/southern Kenya is also robust among the ensemble members (Fig. 9d).

Figure 9e and f display ½PET values for each ensemble member in the two GHA averaging regions. PET is much less variable than precipitation and, over both regions, ½PET values in the 21C simulations are clearly distinguished from 20C values except in December over Tanzania/southern Kenya (Fig. 9f), when the wetting of the surface associated with increased rainfall rates (Fig. 9d) counteracts the greenhouse gas-induced surface warming.

In May, the primary source of moisture over Ethiopia and Somalia is the meridional branch of the Somali jet (Riddle and Cook 2008) but, in the 21C simulation, this moisture transport is not enhanced. Instead, the drying is due to a zonally-uniform northward shift in rainfall that occurs in association with the springtime enhancement of the thermal low. Precipitation is enhanced across the Sahel in May (Figs. 7c, 8a), but not enough to generate GSDs because of high PET rates (Fig. 8a). This northward shift of the rainfall in the eastern Sahel is associated with drying in Ethiopia and Somalia (Fig. 7c). Even if there were no increase in PET, this reduction in rainfall would eliminate GSDs in May (Fig. 9a).

In the Tanzania/southern Kenya region, the boreal spring precipitation anomaly occurs earlier in the season, as does the climatological rainfall maximum, centered in March and April (Fig. 9b). The Somali jet has not begun to form, and the primary source of moisture is zonal onshore flow from the Indian Ocean below about 800 hPa (Fig. 10a). Westerly low-level moisture transport from the equatorial Atlantic supports a Congo basin precipitation maximum to the west. Above 800 hPa, represented by the 700 hPa level in Fig. 10b, the moisture transport is easterly across the continent, as some of the moisture that is converged at lower levels is advected to the west.

Figure 10c shows anomalies for March and April for 21C–20C. Drying over equatorial East Africa is accompanied by increased rainfall to the west. Moisture transport anomalies are small in the lower levels, but at 700 hPa moisture is being transported from the anomalously dry region in the east to the anomalously wet region in the west.

The simulated enhancement of the short rains season in Tanzania and southern Kenya is consistent with results from other models (e.g., Behera et al. 2005, Shongwe et al. 2011) and observational analyses (e.g., Mutai et al. 1998, Black et al. 2003). The presence of the Indian Ocean dipole (Fig. 2) and especially the extensive warming near the east African coast enhances the moisture content of the onshore flow and enhances the short rains.

5.3 Central Africa

Over large parts of tropical central Africa, within 5° of the equator and west of the rift valley, GSDs increase by 20–60 days (5–15%) in the 21C simulation (Fig. 6, Table 3). Figure 11 shows the time series of precipitation and 1/2PET averaged over the strong response at 1.2°S–3.1°N and 11.0°E–20.4°E. This is a region with two growing seasons separated by dry periods in July–August, and December–February in the 20C simulation and in observations. In the 21C simulation, rainfall rates decrease by up to 2 mm/day in the austral spring (October), but this does not influence the GSD calculation. However, the austral summer dry season is shortened to 1 month (December) by rainfall increases of 1–3 mm/day in January and February. There is good agreement among the 6 21C ensemble members on the increase in rainfall in January and February (Fig. 11b), with several peaks in the 21C simulations that are unprecedented in the 20C simulation. As for all of the regions, the response in PET (not shown) is also consistent across the ensemble members.

Figure 11c displays anomalies of precipitation (shading), 900-hPa geopotential height (contours), and 900-hPa moisture transport (vectors) for the January and February mean. The positive precipitation anomaly centered on the equator between 10°E and 30°E that is responsible for the increase in GSDs in tropical central Africa is associated with the convergence of moist southwesterly low-level flow. Geopotential heights over the Sahel are lower in 21C than in 20C, introducing large-scale negative meridional geopotential height anomalies south of 15°N. Very close to the equator, in the absence of strong Coriolis accelerations, these gradients produce the southwesterly flow over the region of enhanced precipitation. North of 10°N, the flow becomes more geostrophic, but close to the equator the ageostrophic flow supports the positive precipitation anomaly.

5.4 Southern Africa

GSDs decrease over almost all of southern Africa in the 21C simulation (Fig. 6). In the southwest, covering Angola and extending into western Zambia, the southern Democratic Republic of Congo (DRC) and Congo, decreases in GSDs range between 30–90 days (40–80%). The entire southeast coast exhibits decreases in GSDs, but the percentages are somewhat smaller.

Figure 12a shows the time series of precipitation and ½PET averaged from 15.6°S–4.6°S and 13.5°E–24.7°E, representing the tropical southwest region of decreased GSDs (Fig. 6). This is a region with bimodal growing seasons and, in the 21C simulation, there is a shortening of the austral fall growing season. The onset is delayed about 16 days due to increases in PET, and there is an early end to the fall growing season of 11 days due to higher evaporation, a decrease in precipitation, and a 2-day reduction in the extension time (Table 3).

There is a complete loss in the austral spring growing season in association with reduced precipitation and increased PET (Fig. 12a, Table 3). In 21C, the spring rains begin in September and early October as in the 20C simulation, but level off in mid October with rainfall rates 1–2 mm/day less than in the 20C simulation. Combined with increases in ½PET of 1–2 mm/day, the criterion that $P > ½\text{PET}$ is never met.

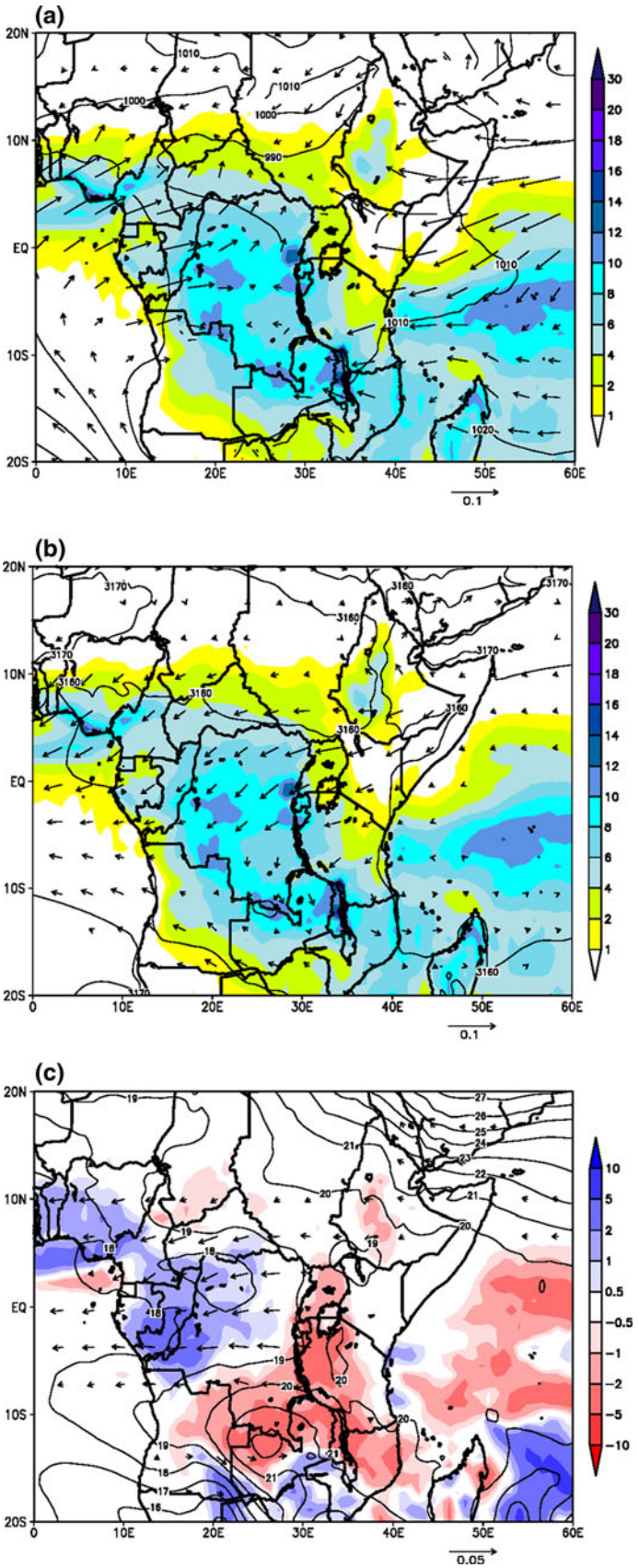

Fig. 10 Precipitation (*shading*), moisture transport (vectors; kg m/kg s), and geopotential heights (contours; gpm) for March/April from the 20C ensemble mean at **a** 900 hPa and **b** 700 hPa. **c** Anomalous precipitation (*shading*), moisture transport (vectors), and geopotential heights (contours) at 700 hPa for March/April for 21C–20C

Table 3 Simulated changes in growing seasons over tropical and southern Africa

Region/season		Start date ($P > 1/2$PET)	End date ($P < 1/2$PET)	Extension[a]	Difference (21C–20C)
Southwest/Spring	20C	October 18	December 19	January 2	−76 days
	21C	None	None	None	
Southwest/Fall	20C	February 22	May 8	May 26	−27 days
	21C	March 10	April 29	May 15	
Southeast[b]	20C	November 2	March 30	April 14	−8 days
	21C	November 5	March 25	April 9	

[a] Estimated date following the date when precipitation falls below 1/2PET on which 100 mm of water stored in the soil has evapotranspired

[b] Decreases in GSDs simulated for the winter season due to unrealistically high winter precipitation in the 20C simulation are not included

There is good agreement among the ensemble members on the early demise to the austral fall rainy season as 5 out of 6 of the 21C integrations produce an earlier end to the season than all of the 20C simulations (not shown). There is less agreement on the delayed fall onset (the March anomaly), which is highly variable in all of the 20C and 21C ensemble members. The precipitation reduction in the spring is captured by all of the 21C ensemble members. Similarly, the increase in PET that contributes to a shortening of the fall growing season is simulated uniformly by the 21C ensemble members, with all of the 21C simulations above the 20C mean and a clear separation between the 2 ensembles (not shown).

Figure 12b displays precipitation, 900-hPa geopotential height anomalies, and 900-hPa moisture transport anomalies averaged over November and December. The loss of the spring growing season in the southwest is associated with a northeast shift of the South Indian convergence zone (SICZ; Cook 2000), which is the time-mean manifestation of the tropical-temperature troughs (TTTs) whose variations characterize the region's rainfall variability on many time scales (e.g., Todd et al. 2004; Fauchereau et al. 2009). The circulation anomaly associated with such a shift transports and converges moisture to the east. This typical mode of variability is often observed, and it has been associated with warming in the Indian Ocean, sometimes with ENSO warm events (e.g., Manhique et al. 2011)

Decreases in GSDs over southeastern Africa have a different seasonality and a different cause from the decreases in GSDs over southwestern Africa. Figure 13a shows the time series of precipitation and ½PET averaged from 26.5°E–31.6°E and 24.5°S–19.7°S, and Fig. 13b and c are time series for the individual ensemble members. (This is a relatively small averaging region chosen to clarify the signal. The response is similar throughout the region, but with slightly different timing). Over southeastern Africa there is one growing season, from November through March, and this growing season is captured in the 20C simulation. But the 20C simulation produces a second short growing season in June when an unobserved secondary precipitation maximum develops. This unobserved precipitation maximum generates about 30 additional growing days and is in large part responsible for the overestimation of GSDs in the southeastern region (Fig. 6). In the 21C simulation, PET increases and precipitation decreases during June and eliminates this false growing season, unrealistically adding to the severity of the simulated loss in GSDs.

It is interesting to note in the context of this analysis that reductions in austral winter precipitation over southern Africa were simulated in the IPCC AR4 coupled GCM with high agreement (IPCC 2007). It was not clear if a similar spurious secondary precipitation maximum was generated in those models in the twentieth century simulations and then eliminated in twenty-first century simulations as in the present study.

Neglecting the spurious simulation of the mid-austral winter growing season, there remains a loss of GSDs over southeastern Africa, but it is not extreme (Table 3). For the southeast averaging region, the onset of the growing season is delayed 3 days, primarily due to increased PET in the greenhouse gas-warmed world, and the end of the rainy season is advanced by 5 days due to precipitation decreases in March. The extension period is unchanged. The increase in PET in spring is captured in all but 1 of the 6 21C ensemble members, but the early end to the rainy season is not robust across the ensemble members (Fig. 13b) since very high variability obscures the signal, in part due to the relatively small averaging region.

6 Summary and conclusions

Regional climate model simulations at 90-km resolution are used to evaluate changes in growing seasons as climate warms under greenhouse gas forcing. A mid-line emissions forcing scenario (SRES A1B) and a target date of the mid–twenty-first century. (2041–2060) are chosen to produce results relevant for impacts analysis and mitigation efforts.

An evaluation of confidence accompanies each regional projection. Confidence, or lack thereof, is based on the

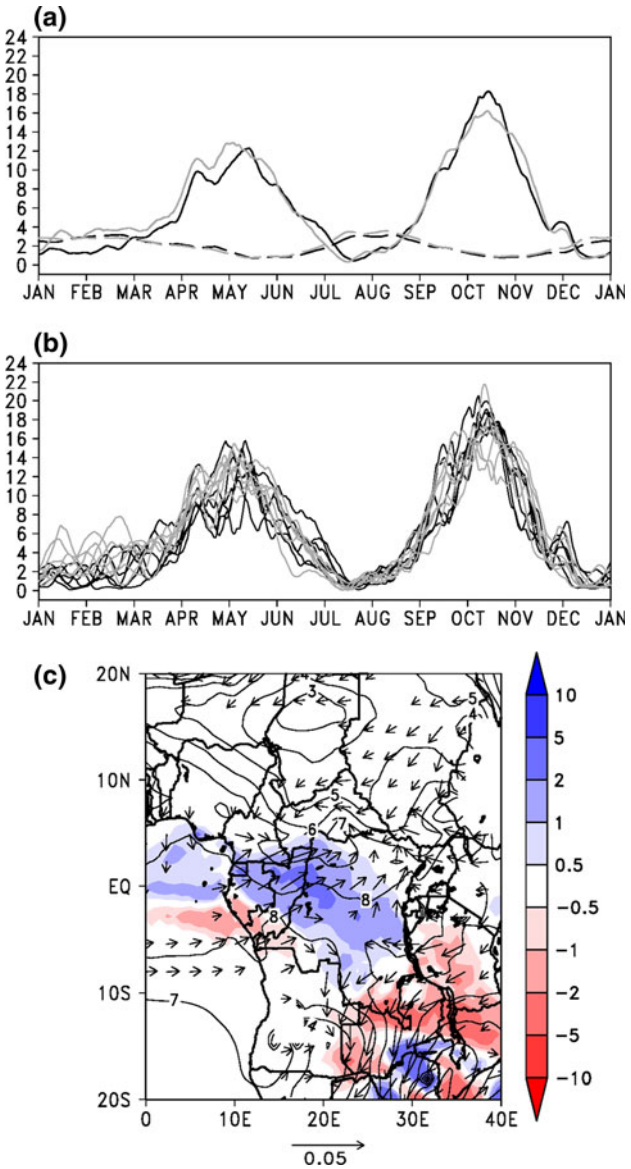

Fig. 11 **a** Annual time series of precipitation (*solid*) and ½PET (*dashed*) in the Congo basin region (11.0°E–20.4°E and 1.2°S–3.1°N) from the 20C (*black*) and 21C (*gray*) ensemble means. **b** Annual time series of precipitation in the Congo region for the 6 20C (*black*) and 6 21C (*gray*) ensemble members. **c** Jan/Feb 21C–20C precipitation (mm/day) and 900 hPa qv (kg m/kg s) differences, and geopotential height anomalies

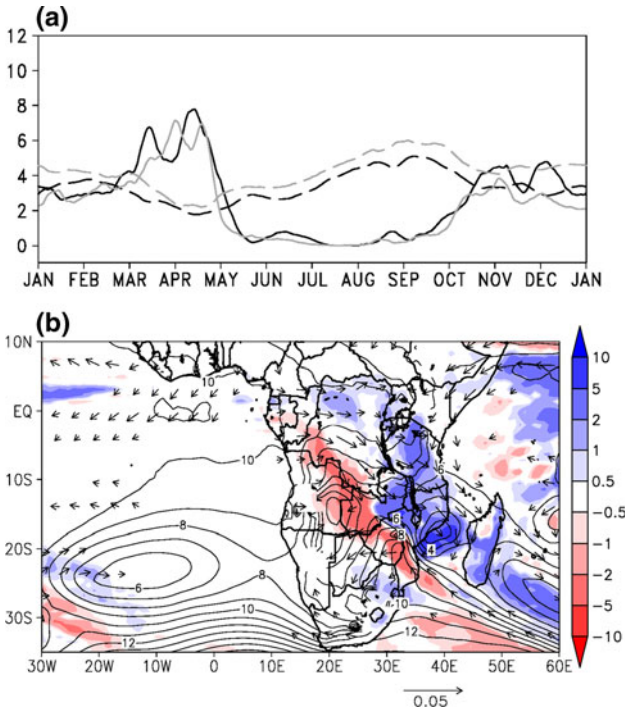

Fig. 12 **a** Annual time series of precipitation (*solid*) and ½PET (*dashed*) in the southwestern region (13.5°E–24.7°E and 15.6°S–4.6°S) from the 20C (*black*) and 21C (*gray*) ensemble means. **b** November/December 21C–20C precipitation (mm/day) and 900 hPa qv (kg m/kg s) differences, and geopotential height anomalies (gpm)

model's ability to simulate the twentieth century climate, agreement among ensemble members, understanding of physical processes, and comparison with other model simulations in the literature.

Results for individual regions where significant changes were simulated are summarized as follows:

- West Africa. The response is highly regional, with decreases in GSDs up to 20% in the western Guinean coast and some regions to the east experiencing 5–10% increases. A westward shift of rainfall in spring is related to an enhanced thermal low over the Sahara.
- Sahel. Increased summer rain and a longer growing season up to 30% in the central and eastern Sahel, with shorter seasons in parts of the western Sahel, also related to a strengthening of the thermal low.
- East Africa (Greater Horn of Africa). The short rains are enhanced as the Indian Ocean warms, with a weak east/west dipole pattern. Enhanced mid-tropospheric moisture divergence in the boreal spring severely curtails the long rains season in Tanzania and southern Kenya, while a northward shift of rainfall in the eastern Sahel eliminates boreal spring GSDs in Somalia and southern Ethiopia.
- Central Africa (Congo basin). Enhanced rainfall in January and February increases the growing season by 5–15% due to enhanced southwesterly moisture transport from the tropical Atlantic.
- Subtropical southwest Africa. In Angola and the southern DRC, severe (40–80%) reductions in the austral spring growing season days are associated with reduced precipitation and increased evapotranspiration. The SICZ shifts to the northeast, leaving the region anomalously dry.

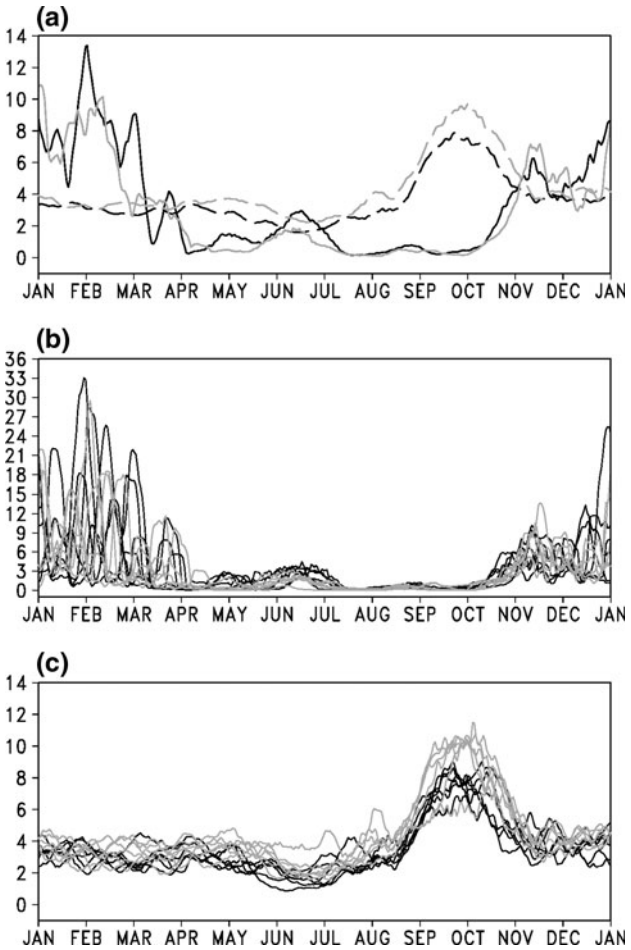

Fig. 13 **a** Southeastern Africa region (26.5°E–31.6°E and 24.5°S–19.7°S) annual time series of precipitation (*solid*) and ½PET (*dashed*) from the 20C (*black*) and 21C (*gray*) ensemble means. Time series of **b** precipitation and **c** ½PET over the southeastern region from each 20C (*black*) and 21C (*gray*) ensemble member. All values have been smoothed using an 11-day run mean. Units are mm/day

- Southeastern Africa. Large-scale reductions in growing season are simulated due to a reduction in winter rainfall that is inaccurate in the 20C simulation. Only small decreases in the actual growing season are simulated when PET increases in the warmer climate.

The region-by-region examination of changes in growing seasons reveal more general insights about how growing seasons may change across Africa as greenhouse gas concentrations increase.

Changes in the thermal low: Under greenhouse gas forcing, the thermal (heat) low is stronger. This has consequences across northern and tropical Africa. May rainfall over West Africa shifts to the east, increasing (decreasing) the length of the boreal spring growing season in eastern (western) West Africa. In the boreal summer, the stronger heat low generates stronger meridional geopotential height gradients and moisture convergence in the eastern and central Sahel, shifting the rainfall northward. This extends the summer growing season in the Sahel, and even introduces some growing days into regions with none in the 20C simulation. But it also induces drying over eastern Ethiopia, Somalia, and the Congo basin which lose growing days.

False drying due to an inaccurate simulation: The case of southeastern Africa in these simulations emphasizes the need for regional analysis. The simulated loss in growing season days is apparently large, but closer investigation reveals that the loss occurs in the austral winter in the simulation—a time when there are few if any growing days in reality. The spurious loss occurs because the model simulation overestimates austral winter precipitation in the 20C simulation, and this winter precipitation is reduced in the 21C simulation.

Role of evapotranspiration changes: There are two factors most important in changing (potential) evapotranspiration in these simulations. One is surface temperature, and the surface temperature increases projected for mid-century under the A1B emissions scenario used here lead to increases in evapotranspiration of about 1–2 mm/day. In isolation, such increases would shorten growing seasons significantly, depending on the region. The other factor that controls evapotranspiration is precipitation, through its influence on soil moisture. Feedbacks from evapotranspiration amplify the effect of negative precipitation anomalies on growing season, but positive precipitation anomalies generally result in reductions in temperature-driven evapotranspiration anomalies. When a primary factor in the simulation of growing seasons is changes in evapotranspiration, confidence is enhanced because its variability is low.

Acknowledgments Discussions with our colleagues, Dr. Joshua Busby and Ms. Kaiba White in the LBJ School of Public Policy at The University of Texas at Austin, greatly improved the application and presentation of the climate model output. Support from the U. S. Army Research Laboratory Minerva Project (contract number W911NF-09-1-0077) and from the US Department of Energy Office of Science (award DE-FG02-08ER64610) is gratefully acknowledged. The Texas Advanced Computing Center (TACC) at the University of Texas at Austin provided the high performance computing resources for the simulations.

Open Access This article is distributed under the terms of the Creative Commons Attribution License which permits any use, distribution, and reproduction in any medium, provided the original author(s) and the source are credited.

References

Adler RF, Huffman GJ, Chang A, Ferraro R, Xie P, Janowiak J, Rudolf B, Schneider U, Curtis S, Bolvin D, Gruber A, Susskind

J, Arkin P (2003) The version 2 global precipitation climatology project (GPCP) monthly precipitation analysis (1979-Present). J Hydrometeor 4:1147–1167

Allen RG, Pereira LS, Raes D, Smith M (1998) Crop evapotranspiration: guidelines for computing crop water requirements. FAO Irrigation and Drainage Paper 56, FAO, ISBN 92-5-104219-5

Behera SK, Luo JJ, Masson S, Delecluse P, Gualdi S, Navarram A, Yamagata T (2005) Paramount impact of the Indian Ocean dipole on the East African short rains: a CGCM study. J Clim 18:4514–4530

Benoit P (1977) The start of the growing season in northern Nigeria. Agric Meteorol 18:91–99

Biasutti M, Sobel AH (2009) Delayed Sahel rainfall and global seasonal cycle in a warmer climate. Geophys Res Lett 36, Art. No. L23707

Black E, Slingo J, Sperber KR (2003) An observational study of the relationship between excessively strong short rains in coastal East Africa and Indian Ocean SST. Mon Weather Rev 131:74–94

Chen F, Dudhia J (2001) Coupling an advanced land-surface/hydrology model with the Penn State/NCAR MM5 modeling system. Part I: model description and implementation. Mon Wea Rev 129:569–585

Chen S-H, Sun W-Y (2002) A one-dimensional time dependent cloud model. J Meteor Soc Japan 80:99–118

Cocheme J, Franquin P (1967) An agroclimatological survey of a semi-arid area in Africa, south of the Sahara. WMO, 86 No 210, TP 110, 136

Cook KH (2000) The South Indian convergence zone and interannual rainfall variability over southern Africa. J Clim 13:3789–3804

Cook KH (2008) Mysteries of Sahel droughts. Nat Geosci 1:647–648

Cook KH, Vizy EK (2008) Effects of twenty-first century climate change on the Amazon rainforest. J Clim 21:542–560

Corbett JD, O'Brien RF, Kruska RJ, Muchugu EI (1995) Agricultural environments of the Greater Horn of Africa: a database and map set for disaster mitigation. 9 pp text, 31 maps, plus database. International Center for Research in AgroForestry, Nairobi, Kenya

Dee DP, Uppala SM, Simmons AJ et al (2011) The ERA-Interim reanalysis: configuration and performance of the data assimilation system. Q J Roy Meteorol Soc 137:553–597

Dudhia J (1989) Numerical study of convection observed during the winter monsoon experiment using a mesoscale two-dimensional model. J Atmos Sci 46:3077–3107

FAO (1978) Report on the agro-ecological zones project. Vol 1: results for Africa. World Soil Resources Report 48/1. FAO, Rome, p 158

Fauchereau N, Pohl B, Reason CJC, Rouault M, Richard Y (2009) Recurrent daily OLR patterns in the Southern Africa/Southwest Indian Ocean region, implications for South African rainfall and teleconnections. Clim Dyn 32:575–591

Hagos SM, Cook KH (2007) Dynamics of the West African monsoon jump. J Clim 20:5264–5284

Hagos SM, Cook KH (2008) Ocean warming and late-twentieth-century Sahel drought and recovery. J Clim 21:3797–3814

Hong S-Y, Noh Y, Dudhia J (2006) A new vertical diffusion package with an explicit treatment of entrainment processes. Mon Wea Rev 134:2318–2341

Huffman GJ, Adler RF, Bolvin DT, Gu G, Nelkin EJ, Bowman KP, Hong Y, Stocker EF, Wolff DB (2007) The TRMM Multi-satellite precipitation analysis: quasi-global, multi-year, combined-sensor precipitation estimates at fine scale. J Hydrometeor 8(1):38–55

IPCC (2007) Climate change 2007: the physical science basis. Contribution of working group I to the fourth assessment. In: Solomon S, Qin D, Manning M, Chen Z, Marquis M, Averyt KB, Tignor M, Miller HL (eds) Report of the intergovernmental panel on climate change. Cambridge University Press, Cambridge, United Kingdom and New York, NY, 996 pp

Kain JS (2004) The Kain-Fritsch convective parameterization: an update. J Appl Meteor 43:170–181

Kanamitsu M, Ebisuzaki W, Woollen J, Yang SK, Hnilo JJ, Fiorino M, Potter GL (2002) NCEP-DOE AMIP-II Reanalysis (R2). Bull Amer Meteor Soc 83:1631–1643

Linacre ET (1977) A simple formula for estimating evaporation rates in various climates, using temperature data alone. Agric Meteorol 18:409–424

Manhique AJ, Reason CJC, Rydlberg L, Fauchereau N (2011) Enso and Indian Ocean sea surface temperatures and their relationships with tropical temperate troughs over Mozambique and the Southwest Indian Ocean. Int J Climatol 31:1–13

Meehl GA, Covey C, Delworth T, Latif M, McAvaney B, Mitchell JFB, Stouffer RJ, Taylor KE (2007) The WCRP CMIP3 multimodel dataset: a new era in climate change research. Bull Amer Meteor Soc 88:1383–1394

Mitchell TD, Jones PD (2005) An improved method of constructing a database of monthly climate observations and associated high-resolution grids. Int J Climatol 25:693–712

Mlawer EJ, Taubman SJ, Brown PD, Iacono MJ, Clough SA (1997) Radiative transfer for inhomogeneous atmosphere: RRTM, a validated correlated-k model for the longwave. J Geophys Res 102(D14):16663–16682

Mutai CC, Ward MN, Colman AW (1998) Towards the prediction of the East Africa short rains based on sea-surface temperature-atmosphere coupling. Int J Climatol 18:975–997

Neupane N, Cook KH (2012) Nonlinear response of Sahel rainfall to Atlantic warming: Potential for abrupt climate change. J Clim (Submitted)

Odekunle TO (2004) Rainfall and the length of the growing season in Nigeria. Int J Climatol 24:467–479

Patricola CM, Cook KH (2007) Dynamics of the West African monsoon under mid-Holocene precessional forcing: regional climate model simulations. J Clim 14:1337–1359

Patricola CM, Cook KH (2010) Northern African climate at the end of the twenty-first century: an integrated application of regional and global climate models. Clim Dyn 35:193–212

Patricola CM, Cook KH (2011) Sub-Saharan Northern African climate at the end of the twenty-first century: Forcing factors and climate change processes. Clim Dyn 37:1165–1188

Riddle EE, Cook KH (2008) Abrupt rainfall transitions over the Greater Horn of Africa: observations and regional model simulations. J Geophys Res Atmos 113:D15109

Rodwell MJ, Hoskins BJ (2001) Subtropical anticyclones and summer monsoons. J Clim 14:3192–3211

Segele ZT, Lamb PJ (2005) Characterization and variability of Kiremt rainy season over Ethiopia. Meteorol Atmos Phys 89:153–180

Shongwe ME, van Oldenborgh GJ, van den Hurk B, van Aalst M (2011) Projected changes in mean and extreme precipitation in Africa under global warming. Part II: East Africa. J Clim 24:3718–3733

Sivakumar MVK (1988) Predicting rainy season potential from the onset of rains in southern Sahelian and Sudanian climatic zones of West Africa. Agric For Meteorol 42:295–305

Skamarock WC, Klemp JB, Dudhia J, Gill DO, Barker DM, Wang W, Powers JG (2005) A description of the advanced research WRF version 2. NCAR/TN-408+STR, 88 pp. Available from NCAR Information Services, P.O. Box 3000, Boulder, CO 80307

Stern RD, Coe R (1982) The use of rainfall models in agricultural planning. Agric Meteorol 26:35–50

Thornthwaite CW (1948) An approach toward a rational classification of climate. Geogr Rev 38:55–94

Thornton PK, Jones PG, Alagarswamy G, Andresen J (2009) Spatial variation of crop yield response to climate change in East Africa. Glob Environ Change 19:54–56

Thornton PK, Jones PG, Ericksen PJ, Challinor AJ (2011) Agriculture and food systems in sub-Saharan Africa in a 4 C+ world. Phil Trans R Soc A 369:117–136

Todd MC, Washington R, Palmer PI (2004) Water vapour transport associated with tropical-temperate trough systems over southern Africa and the southwest Indian Ocean. Int J Climatol 24:55–568

Vigaud N, Roucou P, Fontaine B, Sijikumar S, Tyteca S (2011) WRF/ARPEGE-CLIMAT simulated trends over West Africa. Clim Dyn 35:925–944

Vizy EK, Cook KH (2002) Development and application of a mesoscale climate model for the tropics: Influence of sea surface temperature anomalies on the West African monsoon. J Geophys Res Atmos 107 (D3) doi:10.1029/2001JD000686

Vizy EK, Cook KH (2003) Connections between the summer East African and Indian rainfall regimes. J Geophys Res 108 (D16):4510. doi:10.1029/2003JD003452

Vizy EK, Cook KH (2005) Evaluation of Last Glacial Maximum sea surface temperature reconstructions through their influence on South American climate. J Geophys Res 110:D11105. doi:10.1029/2004JD005415

Vizy EK, Cook KH (2010) Influence of Amazon/Orinoco plume on the summertime Atlantic climate. J Geophys Res 115:D21112. doi:10.1029/2010JD014049

Xie P, Arkin PA (1997) Global precipitation: a 17-year monthly analysis based on gauge observations, satellite estimates and numerical model outputs. Bull Amer Meteor Soc 78:2539–2558